Journal of Biomedical Optics

SPIEDigitalLibrary.org/jbo

Hyperspectral imaging and quantitative analysis for prostate cancer detection

Hamed Akbari
Luma V. Halig
David M. Schuster
Adeboye Osunkoya
Viraj Master
Peter T. Nieh
Georgia Z. Chen
Baowei Fei

SPIE

Hyperspectral imaging and quantitative analysis for prostate cancer detection

Hamed Akbari,[a] Luma V. Halig,[a] David M. Schuster,[a] Adeboye Osunkoya,[b,c,e] Viraj Master,[c] Peter T. Nieh,[c] Georgia Z. Chen,[e] and Baowei Fei[a,d,e]
[a]Emory University, Department of Radiology and Imaging Sciences, Atlanta, 30329 Georgia
[b]Emory University, Department of Pathology, Atlanta, 30329 Georgia
[c]Emory University, Department of Urology, Atlanta, 30329 Georgia
[d]Emory University and Georgia Institute of Technology, Department of Biomedical Engineering, Atlanta, 30329 Georgia
[e]Emory University, Winship Cancer Institute, Atlanta, 30329 Georgia

Abstract. Hyperspectral imaging (HSI) is an emerging modality for various medical applications. Its spectroscopic data might be able to be used to noninvasively detect cancer. Quantitative analysis is often necessary in order to differentiate healthy from diseased tissue. We propose the use of an advanced image processing and classification method in order to analyze hyperspectral image data for prostate cancer detection. The spectral signatures were extracted and evaluated in both cancerous and normal tissue. Least squares support vector machines were developed and evaluated for classifying hyperspectral data in order to enhance the detection of cancer tissue. This method was used to detect prostate cancer in tumor-bearing mice and on pathology slides. Spatially resolved images were created to highlight the differences of the reflectance properties of cancer versus those of normal tissue. Preliminary results with 11 mice showed that the sensitivity and specificity of the hyperspectral image classification method are 92.8% to 2.0% and 96.9% to 1.3%, respectively. Therefore, this imaging method may be able to help physicians to dissect malignant regions with a safe margin and to evaluate the tumor bed after resection. This pilot study may lead to advances in the optical diagnosis of prostate cancer using HSI technology. [DOI: 10.1117/1.JBO.17.7.076005]

Keywords: hyperspectral imaging; prostate cancer; least squares support vector machine; image classification; optical diagnosis.

Paper 11774 received Dec. 20, 2011; revised manuscript received May 24, 2012; accepted for publication Jun. 1, 2012; published online Jul. 6, 2012.

1 Introduction

Hyperspectral imaging (HSI) is an emerging modality for medical applications.[1] This new technology was originally derived from the field of remote sensing, which was developed by NASA for space exploration and earth observation.[2] HSI can extend human vision to infrared and near-infrared wavelength regions. In fact, this imaging system produces several, narrow-band images at different wavelengths. Compared to using conventional color cameras and other filter-based imaging systems, this system produces full neighboring spectral data with both spectral and spatial information.[3] In medical applications, HSI data provide a powerful tool for noninvasive tissue analysis. HSI has also been used to provide quantitative data regarding tissue oxygen saturation in patients with peripheral vascular disease,[4] to detect ischemic regions of the intestine during surgery,[5] to predict and follow healing in foot ulcers of diabetic patients,[6] and to diagnose hemorrhagic shock.[7]

One particularly important application of HSI is the detection of cancer, the second leading cause of death in industrialized countries.[8] Among various cancers, prostate cancer is the cancer most often detected in American men. It is estimated that in 2010 there were 217,730 new cases detected in the United States and that 32,050 American men died of prostate cancer.[8] The current gold standard for definitive diagnosis of prostate cancer is ultrasound-guided biopsy, which involves the removal of tissue samples from the prostate for pathology examination, the results of which, in order to identify a suspected tumor, generally require several days to obtain. Alternatively, as HSI is capable of capturing in one snapshot both the spatial and spectral information for an organ, it could reduce the time required for cancer detection, especially during surgery.

Although HSI has been used to discriminate between cancerous and normal tissue,[9] this method was limited to the visible wavelength range and required the injection of fluorescent material. HSI has also been evaluated for use in the cytologic diagnosis of cancer cells.[10] High-resolution HSI microscopy was also evaluated for its ability to detect abnormalities in skin tissue using hematoxylin and eosin (H&E)-stained preparations of normal and abnormal skin, benign nevi, and melanomas.[11] However, both of these methods are limited to use at the cytological level and in the visible wavelength range, and they require additional procedures for sample preparation. It has been reported that HSI has also been used to detect gastric tumors in human subjects.[12] The spectral signatures of the gastric cancer and noncancerous stomach tissue were created in infrared wavelengths.

The spectral information contained in hyperspectral image data allows the characterization, identification, and classification of different types of tissue. However, several critical issues should be considered when classifying hyperspectral data. Among them are (1) a large data set derived from the high number of spectral channels, (2) the spatial variability of the spectral

Address all correspondence to: Baowei Fei, Emory University, Center for Systems Imaging, Department of Radiology and Imaging Sciences, 1841 Clifton Road NE, Atlanta, GA 30329. Tel: (404) 712-5649; Fax: (404) 712-5689; E-mail: bfei@emory.edu, http://feilab.org

0091-3286/2012/$25.00

signature, and (3) the high cost of true sample labeling.[13] Various image processing methods have been developed in an attempt to resolve the hyperspectral data classification problem. Use of the support vector machine (SVM) offers one of the successful approaches to multispectral data classification.[13–17] The properties of SVMs make them well suited to tackle this classification problem, as they are able to (1) efficiently manage large input spaces, (2) deal with noisy samples in a robust way, and (3) produce sparse solutions (i.e., the decision boundary is expressed as a function of a subset of training samples).

HSI has not been previously reported for use in prostate cancer detection. Spectral measurement and analysis of the prostate have desirable advantages. For example, the measurement can be performed without physical contact and many tissue areas can be evaluated simultaneously. It can also be performed without extracting any tissue. This technique may also be utilized for cancer diagnosis in pathology slides and may save time for both patients and pathologists. HSI could potentially be used to detect residual tumors by surveying and noninvasively examining a vast tissue area and without the need to obtain tissue samples.

In this research, we performed both *in vitro* and *in vivo* HSI experiments, and we propose an SVM method for hyperspectral image classification of prostate tumor tissue. We identify spectral signatures of both normal and cancerous tissue in animals. We will now describe the details of the experiments and methods.

2 Materials and Methods

2.1 *Hyperspectral Imaging Instrumentation*

To capture the hyperspectral image data, we used two CRi camera systems (Caliper, Hopkinton, MA); an *in vivo* imaging system was used for animal scans and a microscopic imaging system was used for scanning pathology slides. The *in vivo* camera system can simultaneously acquire full hyperspectral data from as many as three mice and with 25 μm/pixel resolution in only a few seconds. Inside the system are liquid crystal tunable filters that both block unwanted wavelengths and transmit the required wavelength. It requires only milliseconds to change wavelengths, and there is no noise or vibration. The HSI system generates an x-number of images, where x is user-defined. Each image set contains the measurement of the spectrum of all pixels. The wavelength range of interest is defined as being between 450 and 950 nm and with a 2-nm increment. The image series or spectral cube data contain the spectra of each pixel from 450 to 950 nm, and with each image containing 1.4 million data pixels. Therefore, each pixel in the hyperspectral image has a sequence of reflectance in various spectral wavelengths and the sequence shows the spectral signature of that particular pixel. Figure 1 shows a schematic view of hyperspectral images.

For the animal imaging experiment, the *in vivo* imaging system was used to capture hyperspectral images. The system is a light-tight apparatus that uses a Cermax-type, 300-Watt, Xenon light source. This provides 5600°K that spans the electromagnetic spectrum from 500 to 950 nm. The charge-coupled device (CCD) is a 16-bit, high-resolution, scientific-grade imaging sensor. Four fiberoptic, adjustable illuminator arms yield an even light distribution to the subject. The light radiates from the excitation source and then illuminates the sample. Reflected lights pass through the camera lens to the solid-state, liquid crystal tuning element and finally to the CCD. The excitation and emission filter sliders hold two 50-mm-diameter, long-pass filters. The long-pass filters remove the band light especially from the excitation source. These filters are color-coded so as to indicate the wavelength they represent. The field of view (FOV; length × width) is from 3.4 × 2.5 to 10.2 × 7.6 cm with variable zoom. The resolution is from 25 to 75 μm based on the zoom lens position. The fluence rate, that is, the flow of photons over a set angle, is from 4 to 20 mW/cm^2 based on the light position. The scan time is from 5 s to 1 min.

For the imaging experiment with the pathology slides, the microscope system was used to capture the high-resolution images that allow identification of the subtle spectral differences in tissue. The hyperspectral microscope system utilizes an optimized high-throughput tunable filter. The system has a solid-state tunable filter and its spectral range is from 420 to 720 nm. It uses the Sony ICX285 2/3" format, 1.4-megapixel

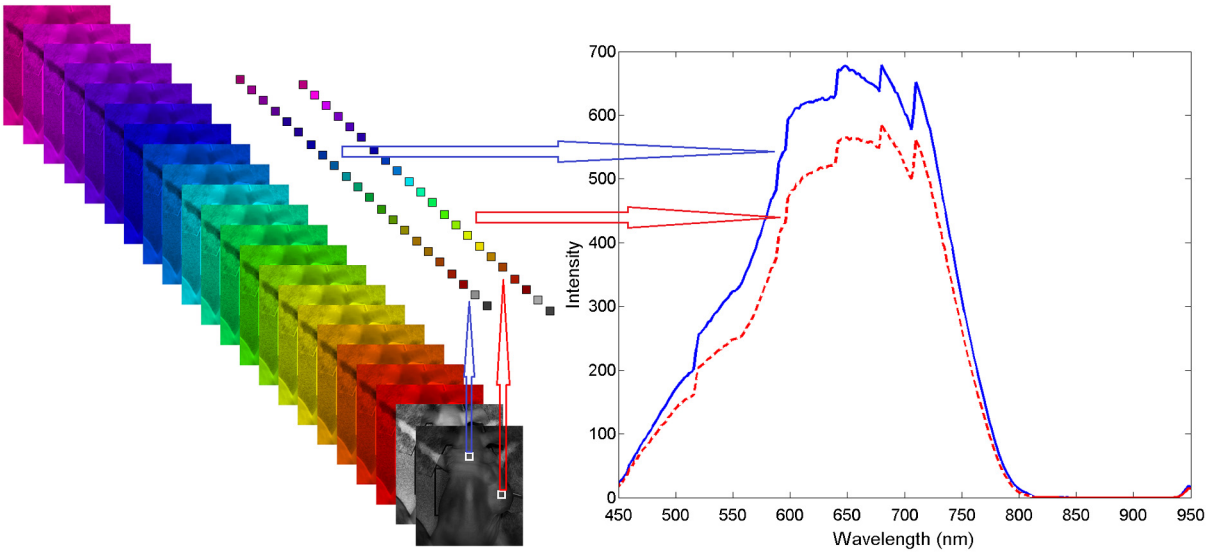

Fig. 1 Schematic view of the hyperspectral images of a nude mouse. Right: the spectral graphs of two, sample pixels from cancer (dashed line) and normal (continuous line) tissue. The graph depicts the normalized reflectance for each wavelength in that pixel. The horizontal axis shows different wavelengths in nanometers. The vertical axis shows the normalized reflectance.

(1392 × 1040 pixels), monochrome progressive scan CCD sensor. Each pixel measures 6.45 μm^2. The system also contains demagnifying optics in front of the CCD and with an effect of 0.63 time magnification. For 40-time magnification, the FOV measures an area of 356.25×266.25 μm^2. In our experiment, we used a 10-time magnification and obtained the 40-time magnification by multiplying the magnification of the oculars. Therefore, the FOV actually measured an area of 3.5625×2.6625 mm^2.

2.2 *Data Normalization*

In order to address the problem of the spectral nonuniformity of the illumination device and the influence of the dark current, the radiance data were normalized to yield the radiance of the specimen. To perform this pre-processing step, the radiance of a standard white reference board was placed in the field of view. The dark currents were measured by keeping the camera shutter closed. The raw data were corrected using the following equation:

$$R(\lambda) = \frac{I_{\text{raw}}(\lambda) - I_{\text{dark}}(\lambda)}{I_{\text{white}}(\lambda) - I_{\text{dark}}(\lambda)}, \quad (1)$$

where $R(\lambda)$ is the calculated reflectance value for each wavelength, $I_{\text{raw}}(\lambda)$ is the raw data radiance value of a given pixel, and $I_{\text{dark}}(\lambda)$ and $I_{\text{white}}(\lambda)$ are the radiance values of the dark current and the white reference board for each spectral band, respectively.

2.3 *Hyperspectral Imaging Experiment in Animals*

An androgen-dependent prostate tumor xenograft model CWR22 was originally derived from a primary human prostatic carcinoma.[18–20] The frozen CWR22 cancer cells were thawed in 37°C water, washed with tissue culture medium (RPMI 1640, Hyclone Laboratories, Inc., Logan, UT) with 20% calf serum (Hyclone Laboratories), and were then filtered through a single layer of Nitex with 100-μm porosity (Tetko, Inc., Briarcliff Manor, NY). The cells were suspended in Matrigel (BD Biosciences, Bedford, MA) with a volume at least equal to that of the cell volume. The suspension was drawn into 1.0-cc syringes with 19-gauge needles for a 0.2-mL volume per injection. Athymic, 4- to 8-week-old nude mice were housed under controlled conditions (12 h dark and light cycles; 20°C to 24°C temperature) and were given freely reachable, sterilized mouse chow. A 12.5-mg, sustained-release, testosterone pellet (Innovative Research of America, Sarasota, FL) was implanted in each nude mouse one week prior to the cell injection. Each animal was given a subcutaneous injection of cell suspension on the other side of the implanted testosterone. The animal experiments were approved by our Institutional Animal Care and Use Committee (IACUC) and conformed to the guidelines of the National Institutes of Health for the care and use of laboratory animals.

In this study, the HSI experiment was performed on 11 male nude mice. Nine mice had human prostate tumors growing on their flanks. During image acquisition, each mouse was anesthetized by intraperitoneal injection of a ketamine and xylazine mixture at a dose of ketamine at 95 mg/kg and xylazine at 5 mg/kg body weight. Figure 2 shows a nude mouse with a prostate tumor.

Fig. 2 A nude mouse with the initiated prostate tumor (arrow).

2.4 *Hyperspectral Imaging Experiment with Pathology Slides*

We used the hyperspectral microscopic imaging system to scan the pathology slides of the prostate obtained from four patients. Each patient underwent prostatectomy. The prostate was surgically removed and sliced at 4-mm intervals. The prostate tissue was then processed histologically. The pathology slides were stained using our standard clinical protocol. The glass slides were analyzed by a pathologist specializing in prostate cancer. The hyperspectral images were captured on the glass slides and were then analyzed using our automatic classification method, as described below. In the imaging experiment, the spectral diagrams of both the tubuloalveolar glands and the fibromuscular stroma were captured for four pathological situations: inflammation, prostatic intraepithelial neoplasia (PIN), Gleason 3, and Gleason 4.

2.5 *Least Squares Support Vector Machine for Hyperspectral Imaging Classification*

As there was a large amount of data for each image, the SVM was used to classify the images. SVM is a data classifier based on statistical learning theory.[15,21] SVM uses a small number of exemplars selected from the training dataset and intended to enhance the generalization ability. It has a pair of margin zones on both sides of the discriminate function. The training phase of SVMs searches for a linear, optimal separating hyperplane as a maximum margin classifier with respect to the training data. However, as training data may not be linearly separable, a kernel-based SVM method was proposed by Camps-Valls and Bruzzone.[13] Kernel-based methods map data from an original input feature space to a kernel feature space of higher dimensionality, after which they then solve a linear problem in that space.

In our study, least squares support vector machine (LS-SVM) is proposed to classify the hyperspectral data. LS-SVM has previously been used for other applications.[13,22–24] This LS-SVM method allows us to interpret and geometrically design learning algorithms in the kernel space that is nonlinearly related to the input space, thus combining statistics and geometry in an effective way. In LS-SVMs, the algorithm attempts to identify a ridge regression for classification using binary targets. Therefore, LS-SVM overcomes some of the disadvantages of classical SVM that attempts to identify a large margin for classification. In LS-SVMs, equality constraints are considered for use with the classification problem and with a formulation in the

least squares sense. As a result, the solution follows directly from solving a set of linear equations instead of quadratic programming.[22]

Given a training set of N data points $\{y_k, x_k\}_{k=1}^{N}$, where $x_k \in R$ is the k'th input pattern and $y_k \in R$ is the k'th output pattern, the SVM approach attempts to construct a classifier of the following form:

$$y(x) = \text{sign}\left[\sum_{k=1}^{N} \alpha_k y_k \Psi(x, x_k) + b\right], \tag{2}$$

where α_k are positive real constants, b is a real constant, and $\Psi(x, x_k) = \exp\{-\|x - x_k\|_2^2/\sigma^2\}$ is the kernel function in the form of the radial basis function form where is constant. The classifier is constructed as follows as one assumes that

$$w^T \varphi(x_k) + b \geq 1, \qquad \text{if } y_k = +1, \tag{3}$$

and

$$w^T \varphi(x_k) + b \geq -1, \qquad \text{if } y_k = -1, \tag{4}$$

where $\varphi(\cdot)$ is a nonlinear function which maps the input space into a higher dimensional space.

In LS-SVM, the classifier is formulated as a least squares problem as described below:

$$\underset{w,b,e}{\text{Min}} f(w, b, e) = \frac{1}{2} w^T w + \gamma \frac{1}{2} \sum_{i=1}^{N} e_k^2, \tag{5}$$

and is subject to the following equality constraints:

$$y_k[w^T \varphi(x_k) + b] = 1 - e_k \qquad k = 1, \ldots, N, \tag{6}$$

where w is the weighting vector, b is the bias term, e is for misclassifications, and γ is the tuning parameter. This constrained optimization problem can be solved by determining the saddle points in the Lagrange function as

$$L(w, b, e; \alpha) = f(w, b, e) - \sum_{k=1}^{N} \alpha_k \{y_k[w^T \varphi(x_k) + b] - 1 + e_k\}, \tag{7}$$

where $\alpha_k \in R$ are Lagrange multipliers, which can be positive or negative in LS-SVM.

The problem can be described as the following linear equations:

$$\begin{bmatrix} I & 0 & 0 & -Z^T \\ 0 & 0 & 0 & -Y^T \\ 0 & 0 & \gamma^I & -I \\ Z & Y & I & 0 \end{bmatrix} \cdot \begin{bmatrix} w \\ b \\ e \\ \alpha \end{bmatrix} = \begin{bmatrix} 0 \\ 0 \\ 0 \\ 1 \end{bmatrix}, \tag{8}$$

where $Z = [\varphi(x_1)^T y_1 \quad \ldots \quad \varphi(x_N)^T y_n]$, $Y = [y_1 \quad \ldots \quad y_n]$, $\rightarrow 1 = [1 \quad \ldots \quad 1]$, and $\alpha = [\alpha_1 \quad \ldots \quad \alpha_N]$. The solution is given by

$$\begin{bmatrix} 0 & -Y^T \\ Y & ZZ^T + \gamma^{-1} I \end{bmatrix} \cdot \begin{bmatrix} b \\ \alpha \end{bmatrix} = \begin{bmatrix} 0 \\ 1 \end{bmatrix}. \tag{9}$$

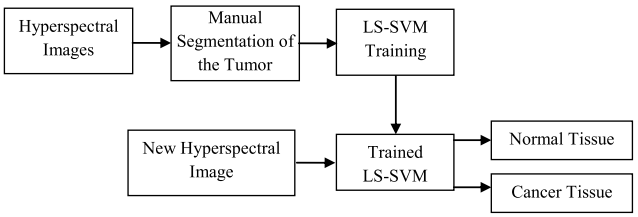

Fig. 3 The flowchart of the tissue classification method for hyperspectral images.

Figure 3 shows the flowchart of our LS-SVM classification method. We first segment the tumor on one group of hyperspectral images for LS-SVM training. For a new group of hyperspectral images, the trained LS-SVM is used to perform the automatic classification of tumors on the new hyperspectral images. We have used input vectors of 251 elements in 2-nm spectral resolution images. The output of the trained LS-SVM is the classification result of normal and cancer tissue on the image.

2.6 *Classification Evaluation*

The automatic classification performance was evaluated with respect to the gold-standard maps created manually by a medical doctor. Sensitivity and specificity were used as statistical measures of the performance of the binary classification method.[25–27] Sensitivity measures the proportion of actual positives that are correctly identified as positive, that is, the percentage of tumor pixels that are correctly identified as tumor tissue. The sensitivity is expressed as follows:

$$\text{Sensitivity} = \frac{\text{TP}}{\text{TP} + \text{FN}}, \tag{10}$$

where TP and FN are true positive and false negative, respectively. When a pixel was not identified as a tumor pixel, the detection was considered as a false negative if the pixel was indeed a tumor pixel in the manually created map. When a pixel was detected as tumor tissue, the detection was classified as a false positive if the pixel was not tumor tissue.

Specificity measures the proportion of negatives that are correctly identified, that is, the percentage of healthy tissue correctly identified as not having cancer. The following equation shows the specificity calculation:

$$\text{Specificity} = \frac{\text{TN}}{\text{TN} + \text{FP}}, \tag{11}$$

where TN and FP are true negative and false positive, respectively.

3 Experiment Results

Figure 2 shows the picture of a tumor-bearing mouse used for the HSI experiment. A total of 11 mice were used for the *in vivo* imaging study. Hyperspectral images were acquired from each mouse. Figure 4 shows the spectral images of a typical mouse. The images obtained at various wavelengths have different sensitivities for detecting the same tumor. Quantitative analysis of the spectral images was performed to compare the spectra of cancer and normal tissue.

As shown in Fig. 5, the spectra of cancer tissue clearly differ from those of normal tissue in the same mouse. It is

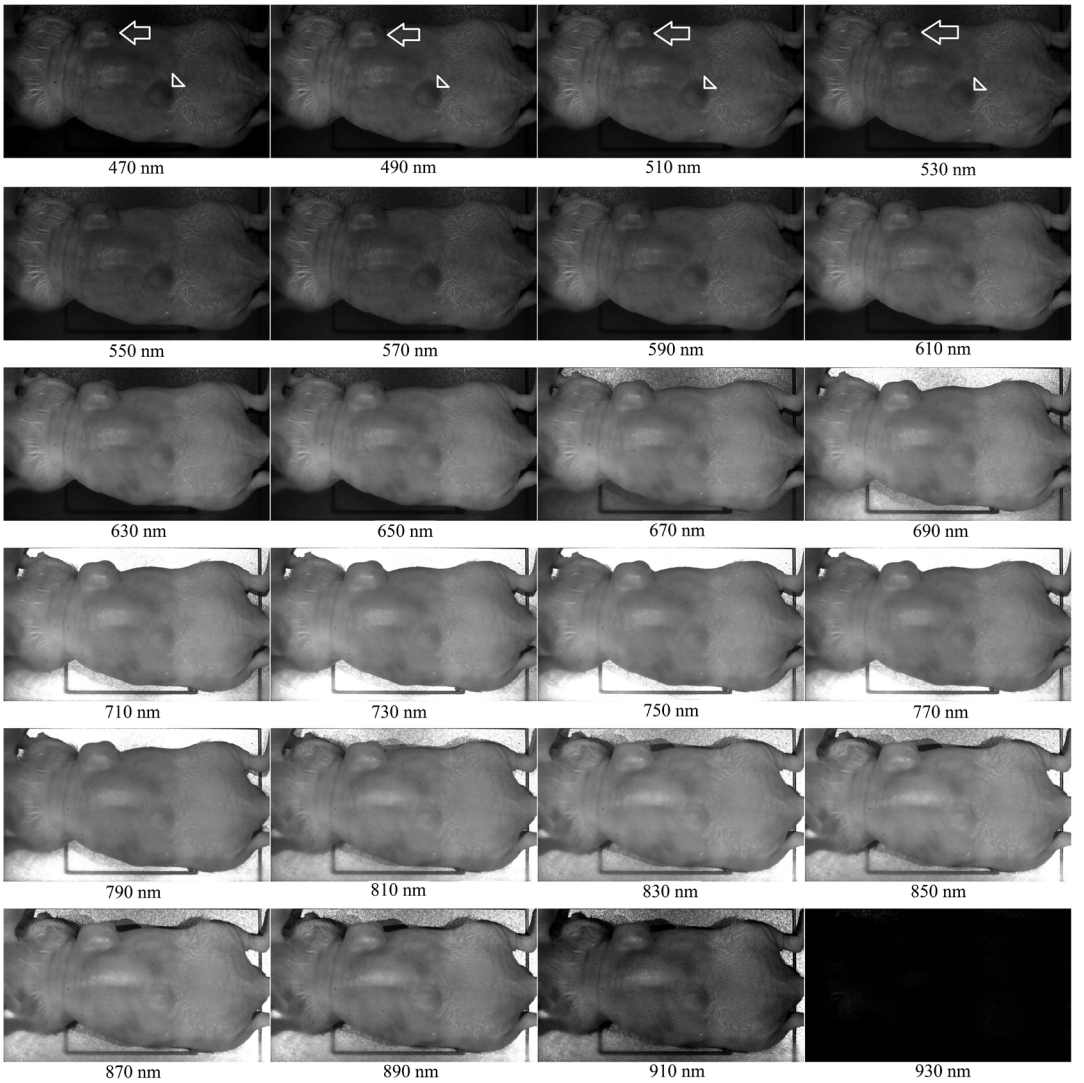

Fig. 4 Spetral images of a tumor-bearing mouse at different wavelengths. The tumor (arrow) and the pellet (arrow head) are visible on the images at various wavelengths.

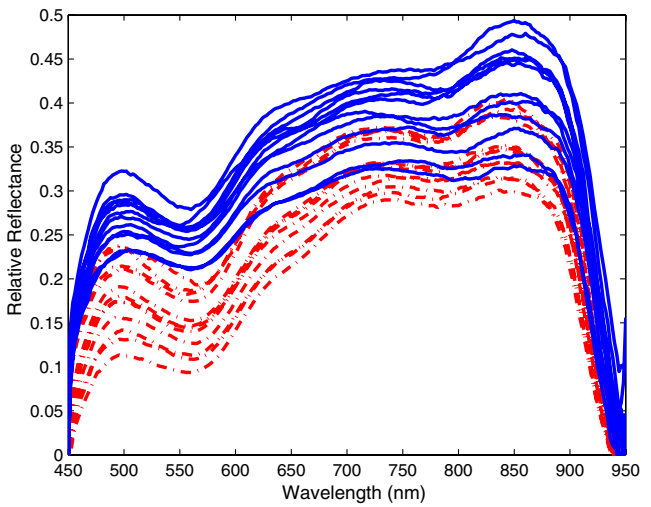

Fig. 5 *In vivo* spectral signature of 12 pixels of cancer tissue (dot-dashed line) and additional 12 pixels of normal tissue (continuous line) in a nude mouse. The horizontal axis shows the different wavelengths in nanometers. The vertical axis shows the relative reflectance.

interesting that the cancer tissue has a relatively low intensity in the wavelength range between 450 and 950 nm. For all of the hyperspectral images, the spectral intensity was calibrated and normalized based on the white reference. The cancer and normal tissue were from the same mouse and were scanned at the same time. Figure 6 shows that the spectrum of cancer tissue differs from that of normal tissue in the same animal. These spectral signatures were used to automatically classify cancer tissue on hyperspectral images.

Our LS-SVM method is able to automatically classify tumor tissue on hyperspectral images. Figure 7 shows a typical classification result for a tumor-bearing mouse. Most tumor tissue was detected using the hyperspectral classification method. Some minor, false-positive areas are also shown on the image. Based on our classification evaluation methods, we computed the sensitivity, specificity, false positive rate (FPR), and false negative rate (FNR) for each animal.

Table 1 shows the quantitative evaluation results of the LS-SVM classification method. Of the 11 mice, 9 had prostate tumors growing on the flank. The sensitivity for the nine mice was $92.8 \pm 2.0\%$ with a minimum and maximum of 89.3%

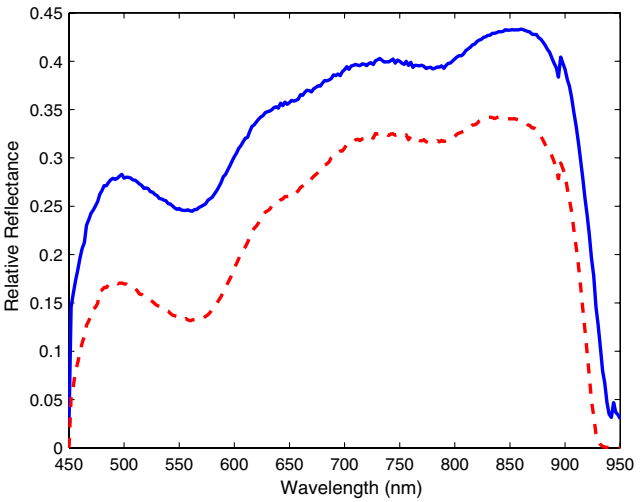

Fig. 6 The mean of the spectral signatures of the cancer tissue (dashed line) and normal tissue (continuous line) in a typical mouse. The horizontal axis shows the different wavelengths in nanometers. The vertical axis shows the relative reflectance.

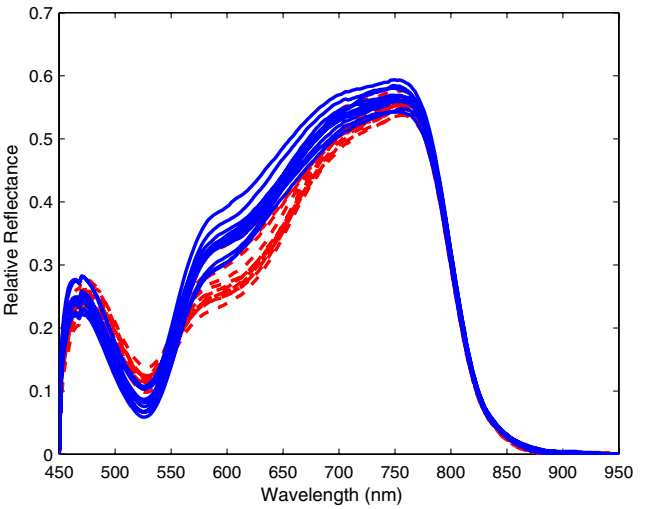

Fig. 8 *In vitro* spectral signature of 10 pixels of cancer tissue (dashed line) and additional 12 pixels of normal tissue (continuous line) seen on pathology slides of a human prostate. The horizontal axis shows the different wavelengths in nanometers. The vertical axis shows the relative reflectance.

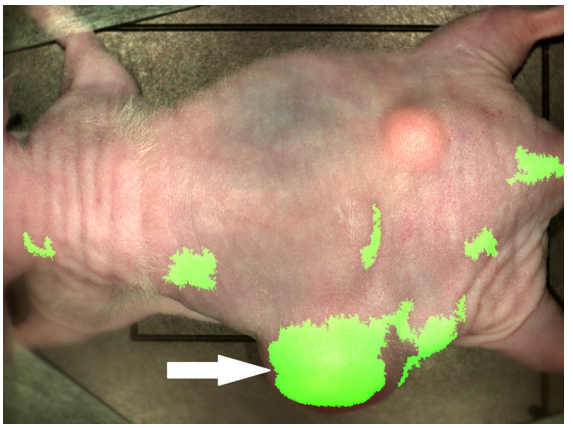

Fig. 7 Detection of cancer tissue (green) in a nude mouse using the proposed classification method. Most of the tumor tissue (arrow) was automatically detected while some false-positive areas are also shown on the image at locations other than the tumor.

and 95.2%, respectively, and which indicates an excellent detection rate of cancer tissue in these animals. The specificity was $96.9 \pm 1.3\%$ with a minimum and maximum of 94.5% and 98.7%, respectively. The false positive and false negative rates are $3.1 \pm 1.3\%$ and $7.2 \pm 2.0\%$, respectively. The quantitative evaluation results demonstrate that the hyperspectral image classification method can automatically detect prostate tumor tissue in mice.

Our *in vitro* HSI experiment also showed interesting preliminary results. Compared to the *in vivo* experiment that imaged tissue in live animals, the *in vitro* experiment obtained spectral images from tissue that had been fixed, processed, and histologically stained. The pathology slides were scanned using the microscopic image system, and high-resolution hyperspectral images were acquired. It is quite interesting that the spectrum of cancer tissue also has a relatively lower intensity than that of normal tissue in the wavelength range between 560 and 770 nm. This is seen in Fig. 8, which shows the spectral profiles of cancer and normal tissue as seen on the pathology slides. Figure 9 shows the mean spectral signatures of cancer and normal tissue, and which indicate the difference between the two tissue types. This preliminary result is consistent with the observation we made in our *in vivo* experiment.

Figure 10 shows one example of the original slide and the classification result. The LS-SVM classification method was used to classify the hyperspectral images of the pathology slides. The original slides were stained with H&E. The cancer tissue was outlined by a pathologist. The hyperspectral classification method was able to detect the tumor region. We also noticed that there are false positive areas on the image. Although this study does not focus on the computer-aided diagnosis of cancer using

Table 1 Sensitivity and specificity of the hyperspectral image classification method used for the detection of prostate cancer tissue in tumor-bearing mice. STD, standard deviation.

Mouse#	1	2	3	4	5	6	7	8	9	10	11	Mean±STD
Specificity (%)	96.7	95.4	97.0	98.7	98.4	98.3	96.4	97.0	97.5	94.5	96.1	96.9±1.3
Sensitivity (%)	93.2	92.0	93.0	95.2	94.4	N/A	N/A	90.5	92.6	89.3	95.0	92.8±2.0
FPR (%)	3.3	4.9	3.0	1.3	1.6	1.7	3.6	3.0	2.5	5.5	3.9	3.1±1.3
FNR (%)	6.8	8.0	7.0	4.8	5.6	N/A	N/A	9.5	7.4	10.7	5.00	7.2±2.0

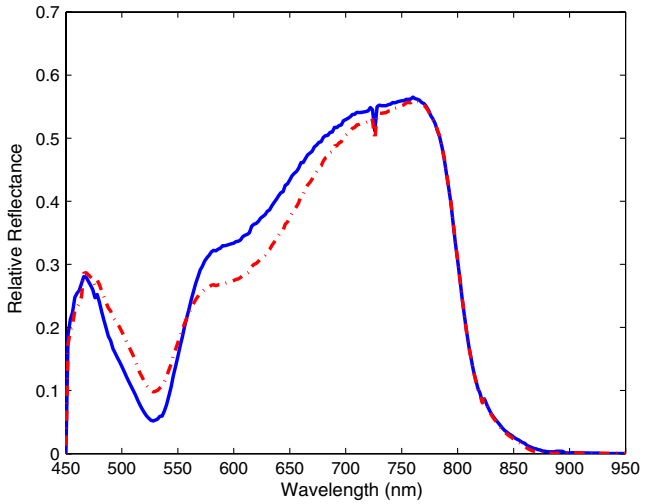

Fig. 9 The mean of spectral signatures of the cancer tissue (dot-dashed line) and normal tissue (continuous line) seen on pathology slides of a human prostate. The horizontal axis shows the different wavelengths in nanometers. The vertical axis shows the relative reflectance.

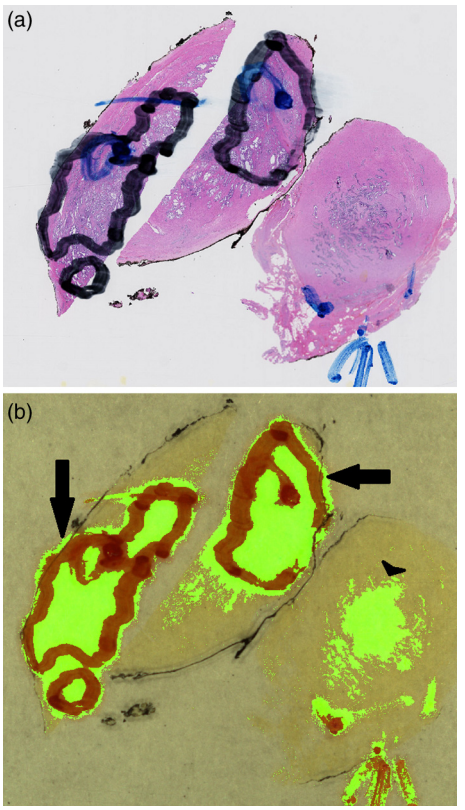

Fig. 10 Automatic detection of cancer tissue on pathology slides using hyperspectral image classification. (a) The original histological slide shows the cancer as outlined by the black line. (b) Most of the cancer tissue (arrows) was detected using the automatic method, while false-postive areas are also shown on the image (arrow head).

images from pathology slides, the method may be used to assist pathologists in making initial estimates.

The high-resolution (6.45 μm), hyperspectral microscopic images can differentiate various tissue types, such as tubulo-alveolar glands and fibromuscular stroma, in the prostate. Figure 11 shows a sample image from a pathology slide

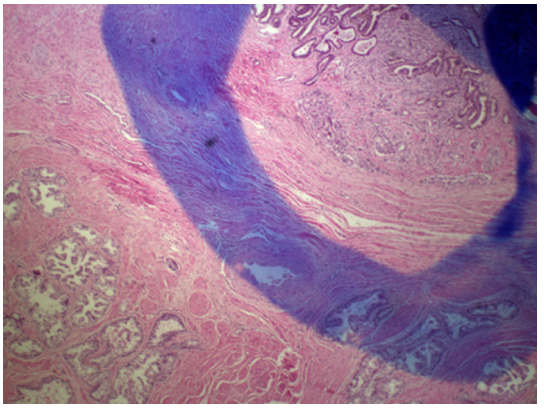

Fig. 11 An RGB image of the hyperspectral microscopic images seen on a pathology slide. The blue line outlining the tumor region was made by a pathologist.

obtained from a patient with prostate cancer. From the pathology slides of our four patients, the spectral diagram of the tubuloal-veolar glands and the fibromuscular stroma was obtained for four pathological situations: inflammations (Fig. 12), prostatic intraepithelial neoplasia (PIN, Fig. 13), Gleason 3 (Fig. 14), and Gleason 4 (Fig. 15). Using hyperspectral microscopic imaging, our pilot results show that cancer and normal tissue have different spectral profiles and that tubuloalveolar glands and fibromuscular stroma demonstrate different spectral signatures. Further investigation will be needed in order to determine why the spectral properties are different for different tissue types.

4 Discussion

In this study, we proposed and evaluated HSI and advanced image processing techniques for cancer detection. The evolving imaging modality HSI may have many potential applications in the medical field. In patients with cancer, if the cancer is

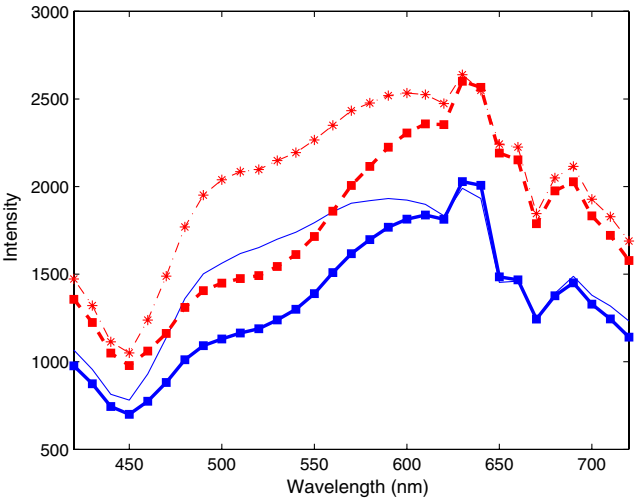

Fig. 12 The spectral diagrams of the normal tubuloalveolar glands (square continuous line), the cancerous tubuloalveolar glands (square dashed line), the normal fibromuscular stroma (continuous line), and the cancerous fibromuscular stroma (star dot-dashed line) seen in prostate inflammation. The horizontal axis shows the different wavelengths in nanometers. The vertical axis shows the intensity of the hyperspectral images.

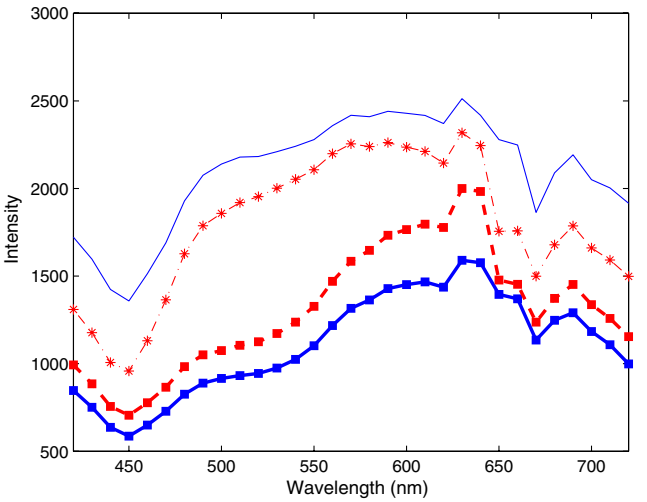

Fig. 13 The spectral diagrams of the normal tubuloalveolar glands (square continuous line), cancerous tubuloalveolar glands (square dashed line), the normal fibromuscular stroma (continuous line), and the cancerous fibromuscular stroma (star dot-dashed line) seen in prostatic intraepithelial neoplasia (PIN). The horizontal axis shows the different wavelengths in nanometers. The vertical axis shows the intensity of the hyperspectral images.

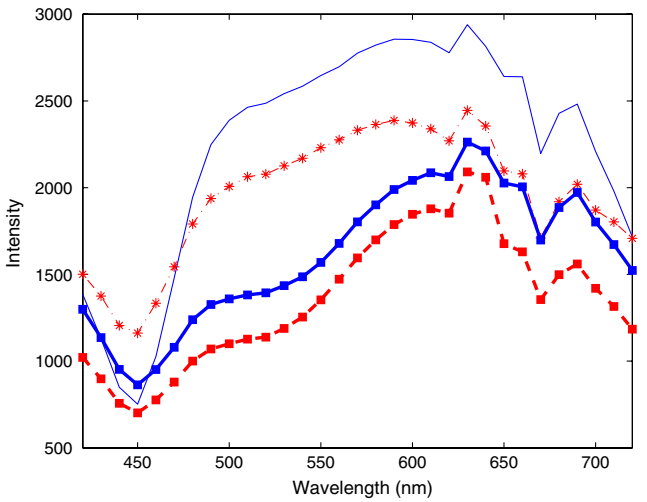

Fig. 14 The spectral diagrams of the normal tubuloalveolar glands (square continuous line), the cancerous tubuloalveolar glands (square dashed line), the normal fibromuscular stroma (continuous line), and the cancerous fibromuscular stroma (star dot-dashed line) seen in prostatic cancer (Gleason 3). The horizontal axis shows the different wavelengths in nanometers. The vertical axis shows the intensity of the hyperspectral images.

diagnosed and treated early, the patient will have a better prognosis and a much greater chance of a full recovery. HSI can be used not only for diagnosis but also to determine the tumor margin. It can be used to evaluate the tumor base following tumor resection in order to ensure that the tumor resection is complete. A safe resection margin can reduce operative mortality and morbidity, reduce the risk of complications and side effects, and, therefore, yield greater long-term patient survival and a significantly more successful treatment outcome.

Crow et al. were among the first researchers who described the use of Raman spectroscopy for prostate disorders.[28] They

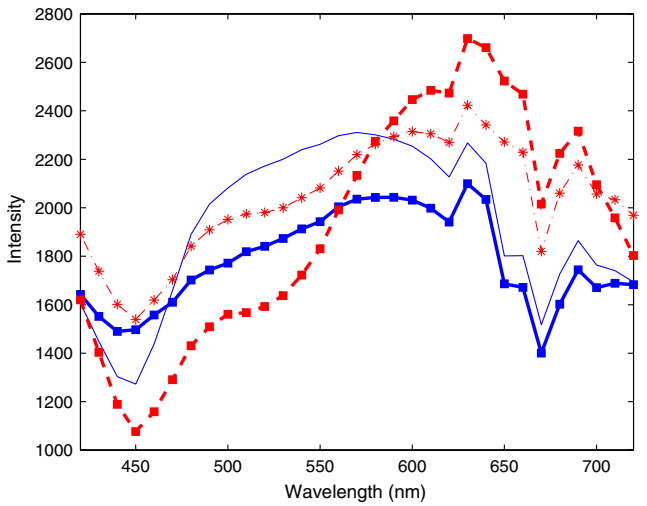

Fig. 15 The spectral diagrams of the normal tubuloalveolar glands (square continuous line), the cancerous tubuloalveolar glands (square dashed line), the normal fibromuscular stroma (continuous line), and the cancerous fibromuscular stroma (star dot-dashed line) seen in prostatic cancer (Gleason 4). The horizontal axis shows the different wavelengths in nanometers. The vertical axis shows the intensity of the hyperspectral images.

proposed that the prostate spectra differ in glycogen and nucleic acid content in benign prostatic hypertrophy (BPH) and adenocarcinoma. They used an *in vitro* spectroscopic method to differentiate between BPH and prostatic adenocarcinoma.[29] *In vitro* spectroscopy was also used to identify BPH and three grades of prostatic adenocarcinoma. Their method was able to differentiate benign samples from prostate cancer with 86% accuracy. Taleb et al. performed *in vitro* spectroscopy of normal prostate cells and malignant prostate metastases to identify the differences between benign and malignant prostatic cells.[30] The spectra of two, well-differentiated, androgen-sensitive cell lines and two, poorly differentiated, androgen-insensitive cell lines were captured in order to differentiate the aggressiveness of prostate cancer. Crow et al. successfully identified the individual cell lines with 98% sensitivity and 99% specificity.[31] Sharma et al. utilized a needle-like, fiberoptic probe for spectroscopy measurements in prostate cancer. The results obtained from 23 prostate specimens showed that the derived hemodynamic parameters and optical properties can serve as successful biomarkers for differentiating tumor tissue from normal tissue in the human prostate.[32] Unlike HSI that captures the image of a large area in a single snapshot, these research studies were limited to measure the spectra of tissue point by point.

Using HSI, a surgeon's visual capability is extended to invisible wavelengths. This technology expands the visual field from the three RGB spectral bands to more than a hundred spectral bands. As the large amount of data in hyperspectral images can be processed to broaden the spectral range, it can provide useful information for surgeons. HSI can also be used as a visual support tool during surgery. For example, by extending the visual field to infrared or far-infrared regions, previously invisible information can be exactly processed and then visually presented to a surgeon during an operation. Spectral data with a wealth of information can be automatically analyzed and quantified in order to aid in the identification of various tissue types.

In this way, the imaging technique can extend a surgeon's visual field and thus help to continuously detect suspicious cancer tissue without interrupting the surgical procedure.

SVMs are being increasingly used in hyperspectral image segmentation, as their performance has been shown to be superior to that of the other available classification methods.[13–,17,33] Using our advanced image processing and classification method, HSI is able to detect tumors without having to inject any imaging agent. It is well known that biological tissue exhibits fluorescent properties when excited by light.[34] It has also been widely reported that fluorescence imaging using various agents can be used to detect various cancers.[35–37] The laser-induced fluorescence technique has also been used to diagnose cancer,[38] and HSI has been used to enhance the cytologic diagnosis of cancer cells.[10]

As HSI can be performed noninvasively, it has distinct advantages over tissue biopsy. Furthermore, HSI can cover a large area of tissue and can detect abnormal lesions, while biopsy specimens can only be taken from a few tissue samples. Our proposed hyperspectral image classification method detects cancerous tissue pixel by pixel. As the detection of one pixel as a cancerous pixel is not dependent on adjacent pixels, it is possible to detect infiltrated cancerous tissue of various shapes and sizes. During surgery, a tissue sample would need to be transported to a pathology laboratory in order to be processed and analyzed by a pathologist. As this entire procedure takes hours, HSI may also be able to save a substantial amount of time during surgery and this would, of course, be a very important advantage.

HSI has the potential to detect important molecular biomarkers of cancer based on their unique spectral signatures.[39] Although the biochemical descriptions of the spectra remain uncertain, it has been shown that the differences between the two, mean spectra are caused by prostate cancer having increased levels of nucleic acids and reduced levels of glycogen.[40]

HSI and advanced machine learning techniques are used to detect prostate cancer in animals and on pathology slides. The hyperspectral camera used in the current setting would need to be modified in order to be able to be used for future clinical applications during laparoscopic and endoscopic procedures. Using other wavelength bands such as 900 to 1700 nm may improve light penetration into deep tissue. For processing hyperspectral data, SVMs can successfully process high-dimensional data. Our LS-SVM method achieved high classification accuracy. During each imaging session, the white reference showed the maximum reflectance in each wavelength as well as at the current temperature. The use of the white reference and dark currents is important for normalizing spectral image intensities. The spatial resolution can be increased by decreasing the distance between the camera and the sample. Although the proposed method focuses on *in vivo* imaging, the idea of the spectral signature may also be used at the microscopic level.

5 Conclusions

We developed a hyperspectral image classification method to be used for cancer detection. An LS-SVM classifier was used to classify cancer tissue in animals and on pathology slides. Our preliminary study has demonstrated the feasibility of using HSI and quantitative analysis methods for prostate cancer detection. HSI offers a potential noninvasive tool that allows surgeons to inspect and assess a large area of tissue without having to take any tissue samples for pathology examination. Moreover, extending a surgeon's visual capability may be a truly significant breakthrough. An advantage of this HSI technique is its capability to spatially and spectrally verify the spectral variations of different tissue types. Therefore, our method allows continuous evaluation of suspicious cancer tissue without interrupting surgery and could, therefore, be used as a virtual biopsy tool. Using this new imaging technique during surgery may provide a new and successful imaging modality for use in early tumor detection.

Acknowledgments

This research is supported in part by NIH grant R01CA156775 (PI: Fei), Georgia Cancer Coalition Distinguished Clinicians and Scientists Award (PI: Fei), Emory Molecular and Translational Imaging Center (NIH P50CA128301), SPORE in Head and Neck Cancer (NIH P50CA128613), and the Atlanta Clinical and Translational Science Institute (ACTSI) that is supported by PHS Grant UL1 RR025008 from the Clinical and Translational Science Award program.

References

1. S. V. Panasyuk et al., "Medical hyperspectral imaging to facilitate residual tumor identification during surgery," *Canc. Biol. Ther.* **6**(3), 439–446 (2007).
2. A. F. H. Goetz, "Three decades of hyperspectral remote sensing of the earth: a personal view," *Remote Sens. Environ.* **113**(Suppl. 1), S5–S16 (2009).
3. H. Akbari et al., "Hyperspectral image segmentation and its application in abdominal surgery," *Int. J. Funct. Inform. Personal. Med.* **2**(2), 201–216 (2009).
4. D. C. Kellicut et al., "Emerging technology: hyperspectral imaging," *Perspect. Vasc. Surg. Endovasc. Ther.* **16**(1), 53–57 (2004).
5. H. Akbari et al., "Detection and analysis of the intestinal ischemia using visible and invisible hyperspectral imaging," *IEEE Trans. Biomed. Eng.* **57**(8), 2011–2017 (2010).
6. L. Khaodhiar et al., "The use of medical hyperspectral technology to evaluate microcirculatory chaves in diabetic foot ulcers and to predict clinical outcomes," *Diabetes Care* **30**(4), 903–910 (2007).
7. L. C. Cancio et al., "Hyperspectral imaging: a new approach to the diagnosis of hemorrhagic shock," *J. Trauma* **60**(5), 1087–1095 (2006).
8. A. Jemal et al., "Cancer statistics, 2010," *CA Cancer J. Clin.* **60**(5), 277–300 (2010).
9. M. E. Martin et al., "Development of an advanced hyperspectral imaging (HSI) system with applications for cancer detection," *Ann. Biomed. Eng.* **34**(6), 1061–1068 (2006).
10. A. M. Siddiqi et al., "Use of hyperspectral imaging to distinguish normal, precancerous, and cancerous cells," *Cancer* **114**(1), 13–21 (2008).
11. D. T. Dicker et al., "Differentiation of normal skin and melanoma using high resolution hyperspectral imaging," *Cancer Biol. Ther.* **5**(8), 1033–1038 (2006).
12. H. Akbari et al., "Cancer detection using infrared hyperspectral imaging," *Cancer Sci.* **102**(4), 852–857 (2011).
13. G. Camps-Valls and L. Bruzzone, "Kernel-based methods for hyperspectral image classification," *IEEE Trans. Geosci. Remote Sens.* **43**(6), 1351–1362 (2005).
14. G. Camps-Valls et al., "Robust support vector method for hyperspectral data classification and knowledge discovery," *IEEE Trans. Geosci. Remote Sens.* **42**(7), 1530–1542 (2004).
15. M. Brown, H. G. Lewis, and S. R. Gunn, "Linear spectral mixture models and support vector machines for remote sensing," *IEEE Trans. Geosci. Remote Sens.* **38**(5), 2346–2360 (2000).
16. M. Brown, S. R. Gunn, and H. G. Lewis, "Support vector machines for optimal classification and spectral unmixing," *Ecol. Model.* **120**(2–3), 167–179 (1999).

17. F. Melgani and L. Bruzzone, "Classification of hyperspectral remote sensing images with support vector machines," *IEEE Trans. Geosci. Remote Sens.* **42**(8), 1778–1790 (2004).
18. H. Wang and B. W. Fei, "Diffusion-weighted MRI for monitoring tumor response to photodynamic therapy," *J. Magn. Reson. Imaging* **32**(2), 409–417 (2010).
19. B. W. Fei et al., "Choline PET for monitoring early tumor response to photodynamic therapy," *J. Nucl. Med.* **51**(1), 130–138 (2010).
20. B. W. Fei et al., "High-field magnetic resonance imaging of the response of human prostate cancer to Pc 4-based photodynamic therapy in an animal model," *Lasers Surg. Med.* **39**(9), 723–730 (2007).
21. V. N. Vapnik, *The Nature of Statistical Learning Theory*, Springer-Verlag, Berlin (1995).
22. J. A. K. Suykens and J. Vandewalle, "Least squares support vector machine classifiers," *Neural Processing Lett.* **9**(3), 293–300 (1999).
23. Z. Liu et al., "Automated tongue segmentation in hyperspectral images for medicine," *Appl. Opt.* **46**(34), 8328–8334 (2007).
24. T. V. Gestel et al., "Benchmarking least squares support vector machine classifiers," *Mach. Learn.* **54**(1), 5–32 (2004).
25. H. S. Wang and B. W. Fei, "A modified fuzzy C-means classification method using a multiscale diffusion filtering scheme," *Med. Image Anal.* **13**(2), 193–202 (2009).
26. X. F. Yang and B. W. Fei, "A multiscale and multiblock fuzzy C-means classification method for brain MR images," *Med. Phys.* **38**(6), 2879–2891 (2011).
27. K. Bogie et al., "New technique for real-time interface pressure analysis: getting more out of large image data sets," *J. Rehabil. Res. Dev.* **45**(4), 523–535 (2008).
28. P. Crow et al., "The use of Raman spectroscopy to differentiate between different prostatic adenocarcinoma cell lines," *Br. J. Cancer* **92**(12), 2166–2170 (2005).
29. P. Crow et al., "Assessment of fiberoptic near-infrared Raman spectroscopy for diagnosis of bladder and prostate cancer," *Urology* **65**(6), 1126–1130 (2005).
30. A. Taleb et al., "Raman microscopy for the chemometric analysis of tumor cells," *J. Phys. Chem. B* **110**(39), 19625–19631 (2006).
31. P. Crow et al., "The use of Raman spectroscopy to differentiate between different prostatic adenocarcinoma cell lines," *Br. J. Cancer* **92**(12), 2166–2170 (2005).
32. V. Sharma et al., "Optical reflectance spectroscopy for detection of human prostate cancer," *Conf. Proc. IEEE. Eng. Med. Biol. Soc.*, 118–121 (2009).
33. C. Huang, L. S. Davis, and J. R. G. Townshend, "An assessment of support vector machines for land cover classification," *Int. J. Remote Sens.* **23**(4), 725–749 (2002).
34. S. Andersson-Engels et al., "In vivo fluorescence imaging for tissue diagnostics," *Phys. Med. Biol.* **42**(5), 815–824 (1997).
35. N. G. Dolloff et al., "Spectral imaging-based methods for quantifying autophagy and apoptosis," *Canc. Biol. Ther.* **12**(4), 349–356 (2011).
36. Y. Cheng et al., "Highly efficient drug delivery with gold nanoparticle vectors for in vivo photodynamic therapy of cancer," *J. Am. Chem. Soc.* **130**(32), 10643–10647 (2008).
37. Y. Urano, "Sensitive and selective tumor imaging with novel and highly activatable fluorescence probes," *Anal. Sci.* **24**(1), 51–53 (2008).
38. S. K. Chang et al., "Combined reflectance and fluorescence spectroscopy for in vivo detection of cervical pre-cancer," *J. Biomed. Opt.* **10**(2), 024031 (2005).
39. R. T. Kester et al., "Real-time hyperspectral endoscope for early cancer diagnostics," *Proc. SPIE* **7555**, 75550A (2010).
40. P. Crow et al., "The use of Raman spectroscopy to identify and grade prostatic adenocarcinoma in vitro," *Br. J. Cancer* **89**(1), 106–108 (2003).